The University of Sydney

School of Civil Engineering
Sydney NSW 2006
AUSTRALIA

http://www.civil.usyd.edu.au/

Centre for Advanced Structural Engineering

Isoparametric Spline Finite Strip Method for the Bending of Perforated Plates

Research Report No R877

Gabriele Eccher MEng
Kim J. R. Rasmussen MScEng PhD
Riccardo Zandonini MEng PhD

February 2007

The University of Sydney

School of Civil Engineering
Centre for Advanced Structural Engineering
http://www.civil.usyd.edu.au/

Isoparametric Spline Finite Strip Method for the Bending of Perforated Plates

Research Report No R877

Gabriele Eccher MEng
Kim J. R. Rasmussen MScEng PhD
Riccardo Zandonini MEng PhD

February 2007

Abstract:
In a previous report [1], the isoparametric spline finite strip method was successfully applied to the in-plane stress linear elastic analysis of perforated thin-walled structures. In the present report the application of the isoparametric spline finite strip method is further extended to the bending of perforated plates.

The general theory of the isoparametric spline finite strip method is briefly introduced while the development of the Mindlin bending theory and its matrices are discussed in detail.

The reliability of the method is demonstrated by comparisons with finely meshed finite element analyses. Square plates in bending containing openings of different shapes are analysed.

Keywords:
Plate bending analysis, isoparametric spline finite strip method, perforations, thin-walled elements.

Copyright Notice

School of Civil Engineering, Research Report R877
Isoparametric Spline Finite Strip Method for the Bending of Perforated Plates

G.Eccher@civil.usyd.edu.au, K.Rasmussen@civil.usyd.edu.au and Riccardo.Zandonini@ing.unitn.it

Published by:
School of Civil Engineering
The University of Sydney
Sydney NSW 2006
AUSTRALIA

February 2007

This report and other Research Reports published by The School of Civil Engineering are available on the Internet:

http://www.civil.usyd.edu.au

Table of Contents

Introduction

The Spline Finite Strip Method was developed from the semi-analytical Finite Strip Method originally derived by Cheung [2]. The Finite Strip Method was based on harmonic functions, and proved to be an efficient tool for analysing structures with constant geometrical properties along a particular direction, generally the longitudinal one. The spline finite strip method complemented the semi-analytical finite strip method by allowing more complex types of loading and support conditions to be modelled at the expense of a more comprehensive set of displacement functions based on splines. Initially introduced for the static linear and free vibration analyses of flat plates [3], the spline finite strip method was fully developed for the linear elastic structural analysis of folded plate structures by Fan and Cheung [4]. Subsequently, the isoparametric concept was applied to the spline finite strip method by Au and Cheung for the linear in-plane stress and bending analyses of Mindlin plates [5] and degenerated shells [6]. This extension allowed structures having a distorted longitudinal axis to be efficiently analysed with the finite strip method.

The present work originates from the industrial and civil applications of thin-walled structural members with perforations, which can be modelled as complex systems of thin plates. Holes and cut-outs of various shapes are used in practice to ease the assembly of structures [7], or to allow the passage of services, but introduce discontinuities in the cross-section and, consequently, a redistribution of the membrane stresses within the members. Extensive research has been undertaken in the last two decades studying the behaviour of thin plates containing cut-outs of different shapes [8], beams with holes in the web [9] and industrial rack uprights with closely spaced cut-outs [10], highlighting the complexity of the analysis of such structures. The shape of the hole, its position within the cross-section, its dimensions and its longitudinal spacing [11] are the most important parameters defining the global behaviour of the member but it is difficult to combine these factors into simple design guidelines for predicting the ultimate strength. Existing design rules are therefore empirical and only valid in the parameter ranges investigated.

Within this general framework, the authors aim to develop an efficient numerical tool that applies the efficiency of the isoparametric spline finite strip method to the complex analysis of perforated thin-walled structures. In this report the theoretical background for the plate bending analysis by isoparametric spline finite strip method is presented. The isoparametric spline finite strip method is briefly described as a special development of the more general finite strip method. The kinematics assumptions, strain-displacement relations, along with the stress-strain relations, are presented in terms of the displacement functions described in the aforementioned method. The derivation of the corresponding strain and stiffness matrices and load vector is highlighted.

Numerical examples are given to illustrate the accuracy of the method. The examples concern the analysis of perforated plates subjected to bending loads.

Kirchhoff and Mindlin theories

The classical plate bending theories are the Kirchhoff theory for thin plates and the Mindlin theory for moderately thick plates. The principal assumption made in both theories is that plane sections remain plane after deformation, as shown in Fig. 1. In thin plate applications, i.e. in the Kirchhoff theory for plate bending, it is additionally assumed that plane sections, originally orthogonal to the middle surface, remain orthogonal to it after deformation. According to this assumption, along with the assumption of small displacements and deformations, it is possible to establish a direct correspondence between the slopes of the middle plane of the deformed plate, θ_x and θ_y, and the derivatives of the out-of-plane displacement, w:

$$\theta_x = -\frac{\partial w}{\partial x} \tag{1}$$

$$\theta_y = -\frac{\partial w}{\partial y} \tag{2}$$

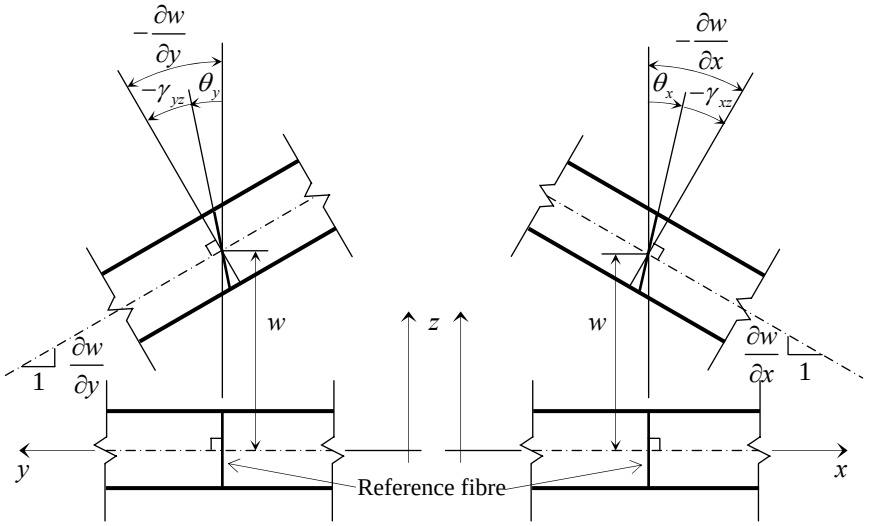

Fig. 1: Plate kinematics for Mindlin and Kirchhoff theory.

The relevant strains in a general bending problem are given by the transverse curvature, χ_{xx}, the longitudinal curvature, χ_{yy}, the twisting curvature, χ_{xy}, and by the two out-of-plane shear strains, γ_{xz} and γ_{yz}. They are expressed by

$$\chi_{xx} = \frac{\partial \theta_x}{\partial x} \tag{3}$$

$$\chi_{yy} = \frac{\partial \theta_y}{\partial y} \tag{4}$$

$$\chi_{xy} = \frac{\partial \theta_x}{\partial y} + \frac{\partial \theta_y}{\partial x} \tag{5}$$

$$\gamma_{xz} = \frac{\partial w}{\partial x} + \theta_x \tag{6}$$

$$\gamma_{yz} = \frac{\partial w}{\partial y} + \theta_y \tag{7}$$

and by substituting (1) and (2) in (3)-(7) we obtain for the Kirchhoff theory,

$$\chi_{xx} = -\frac{\partial^2 w}{\partial x^2} \tag{8}$$

$$\chi_{yy} = -\frac{\partial^2 w}{\partial y^2} \tag{9}$$

$$\chi_{xy} = -2\frac{\partial^2 w}{\partial x \partial y} \tag{10}$$

$$\gamma_{xz} = 0 \tag{11}$$

$$\gamma_{yz} = 0 \tag{12}$$

By inspection of (8)-(12), we note that the out-of-plane strains, γ_{xz} and γ_{xy}, are identically zero and that the bending of the plate can be described simply by means of the deflection of the middle surface of the plate, *w*.

It is important to note that (8), (9) and (10) involve second order derivatives. The consequences of such a formulation are twofold. The finite strip method (as for the finite element method) requires a degree of continuity in the shape functions across the adjoining strips (or elements), equal to the maximum order of the derivatives involved in the relevant strain definition, minus one. In this case, the continuity class required is C^1, a requirement that is not easily fulfilled. Secondly, in (8), (9) and (10), the derivatives are performed with regard to the local coordinates, *x* and *y*, while the displacement functions which represent the deflection, w, are expressed in natural coordinates, ξ and η. Establishing a correspondence between the second order derivatives and the natural coordinates for general geometries is extremely cumbersome. For these reasons, the Mindlin plate theory is more often employed, even in thin plate applications in finite element and finite strip applications.

The Mindlin plate bending theory was originally developed to analyse the bending behaviour of moderately thick plates, where the conditions given in (11) and (12) are not fulfilled and the shear deformability of the plate has to be taken into account. The main assumptions made are that plane sections remain plane after deformation, but sections originally orthogonal to the middle surface of the plate are no longer orthogonal after deformation (Fig. 1). No direct relations, such as those in (1) and (2), can hence be established between middle surface slopes, θ_x and θ_y, and the deflection, *w*. The strain-displacement relations utilised in the Mindlin theory are those given in (3)-(7) where now

three independent functions are involved in the formulation, the out-of-plane displacement of the middle surface, w, and the two rotations, θ_x and θ_y. It is important to underline that, according to this approach, the strain-displacement relations only involve first order derivatives. Consequently, the continuity requirements for the convergence of the finite strip (or finite element) method amount to ensuring a continuity of class C^0 within and across strips (or elements). Furthermore, it is possible to establish a correspondence between the derivatives with respect to the local coordinates, x and y, as present in (3)-(7), and the natural coordinates, ξ and η, in which the displacement functions are defined, simply by use of the Jacobian matrix, as defined in a previous report [1].

In the following, the implementation of the Mindlin plate bending theory in the isoparametric spline finite strip method is presented.

Isoparametric Spline Finite Strip Method

A finite strip is a particular type of finite element, geometrically characterized by having one dimension, the longitudinal one, much greater than the transverse one. The shape functions defined over a plane finite strip differ from those of the plane finite element because the former are expressed in terms of a combination of two families of functions, one depending on the transverse coordinate and one on the longitudinal coordinate. For a bi-dimensional finite strip, the transverse shape functions generally correspond to the finite element shape functions utilized in one-dimensional elements, while trigonometric, exponential or spline series may be utilized for the longitudinal shape functions. Within a finite strip, the nodes are distributed along longitudinal paths called nodal lines. The number of nodes along each nodal line depends on the number of the longitudinal series components, while the number of nodal lines defining a strip is determined by the order of the transverse shape functions, i.e. two nodal lines for linear shape functions, three for quadratic, four for cubic and so on.

In the present work, Lagrangian cubic transverse shape functions and cubic B_3-Spline longitudinal series functions have been utilized.

The transverse cubic shape functions are given by

$$L_1(\xi) = -\frac{9}{16}\left(\xi^3 - \xi^2 - \frac{1}{9}\xi + \frac{1}{9}\right) \tag{13}$$

$$L_2(\xi) = \frac{27}{16}\left(\xi^3 - \frac{1}{3}\xi^2 - \xi + \frac{1}{3}\right) \tag{14}$$

$$L_3(\xi) = -\frac{27}{16}\left(\xi^3 + \frac{1}{3}\xi^2 - \xi - \frac{1}{3}\right) \tag{15}$$

$$L_4(\xi)=\frac{9}{16}\left(\xi^3+\xi^2-\frac{1}{9}\xi-\frac{1}{9}\right) \tag{16}$$

where $L_i(\xi)$ is the component of the shape functions referring to the i^{th} nodal line of the strip and ξ is the transverse curvilinear coordinate. A graphic representation of the transverse shape functions is given in Fig. 2. It follows that the finite strip utilized in the present work is defined by a set of four nodal lines.

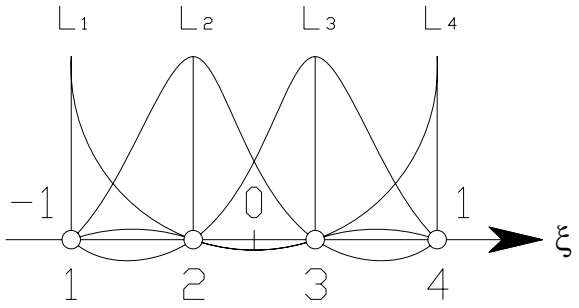

Fig. 2: Cubic transverse shape functions.

The general component of the B_3-Spline series is expressed by

$$\phi_j(\eta)=\frac{1}{6}\begin{cases}0 & ,\ \eta<\eta_{j-2}\\ \left(\eta-\eta_{j-2}\right)^3 & ,\ \eta_{j-2}\le\eta<\eta_{j-1}\\ 1+3\left(\eta-\eta_{j-1}\right)+3\left(\eta-\eta_{j-1}\right)^2-3\left(\eta-\eta_{j-1}\right)^3 & ,\ \eta_{j-1}\le\eta<\eta_j\\ 1+3\left(\eta_{j+1}-\eta\right)+3\left(\eta_{j+1}-\eta\right)^2-3\left(\eta_{j+1}-\eta\right)^3 & ,\ \eta_j\le\eta<\eta_{j+1}\\ \left(\eta_{j+2}-\eta\right)^3 & ,\ \eta_{j+1}\le\eta<\eta_{j+2}\\ 0 & ,\ \eta>\eta_{j+2}\end{cases} \tag{17}$$

where $\phi_j(\eta)$ represents the j^{th} component of the cubic spline series and η is the longitudinal curvilinear coordinate. Its shape is shown in Fig. 3(a). In (17), the indexed longitudinal curvilinear coordinates, η_j, are the coordinates of the nodes which are spaced by a unit distance. By inspection of (17) and Fig. 3(a), it follows that the generic j^{th} spline component is defined over four consecutive sections and centered on the j^{th} node. A full B_3-Spline series comprises m+3 components, i.e. m+3 nodes per nodal line, as shown in Fig. 3(b), where with "m" we denote the number of sections subdividing the strip and, consequently, each nodal line. It also follows that the coordinate η spans from zero to m between the two ends.

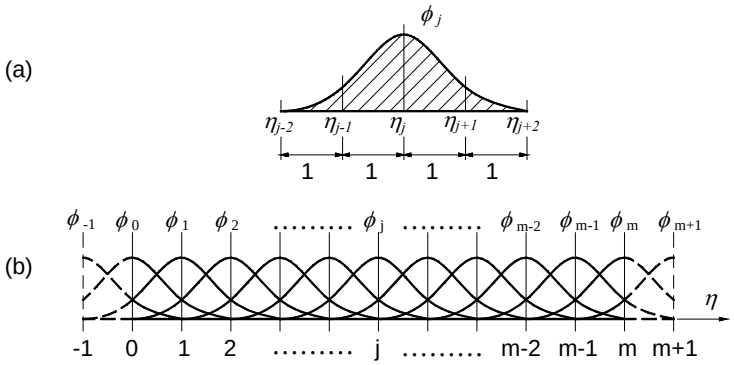

Fig. 3: (a) - j-th component of the B_3-Spline; (b) – a complete B_3-Spline series.

The general displacement function defined within a strip of uniform thickness, *t*, can be expressed in terms of the curvilinear coordinate system by the B_3-spline and Lagrangian shape functions as follows

$$\delta(\xi,\eta)=\sum_{i=1}^{4}\sum_{j=-1}^{m+1}L_i(\xi)\,\phi_j(\eta)\,\alpha_{ij}^{\delta} \tag{18}$$

where δ represents the generic generalized displacement function and the numerical coefficient α_{ij}^{δ} represents the generalized variable which refers to the displacement function δ on the i^{th} nodal line and at the j^{th} node.

Introducing now the shape function N_{ij} as

$$N_{ij}(\xi,\eta)=L_i(\xi)\,\phi_j(\eta) \tag{19}$$

a compact formulation of the general displacement function is given by

$$\delta(\xi,\eta)=\sum_{i=1}^{4}\sum_{j=-1}^{m+1}N_{ij}(\xi,\eta)\,\alpha_{ij}^{\delta} \tag{20}$$

It is convenient to introduce a matrix formulation for the general displacement field δ as follows

$$\delta=\mathbf{N}\,\boldsymbol{\alpha} \tag{21}$$

where

$$\mathbf{N}=\begin{bmatrix}\mathbf{N}_1 & \mathbf{N}_2 & \mathbf{N}_3 & \mathbf{N}_4\end{bmatrix} \tag{22}$$

$$\boldsymbol{\alpha}=\begin{bmatrix}\boldsymbol{\alpha}_1^{\delta T} & \boldsymbol{\alpha}_2^{\delta T} & \boldsymbol{\alpha}_3^{\delta T} & \boldsymbol{\alpha}_4^{\delta T}\end{bmatrix}^T \tag{23}$$

In (22) and (23) the generic sub-matrix $\mathbf{N}_i$ and the sub-vector $\boldsymbol{\alpha}_i^{\delta}$ are given by

$$\mathbf{N}_i = L_i(\xi)\left[\phi_{-1}(\eta) \quad \phi_0(\eta) \quad \phi_1(\eta) \quad \cdots \quad \phi_m(\eta) \quad \phi_{m+1}(\eta)\right] \tag{24}$$

$$\boldsymbol{\alpha}_i^{\delta} = \left[\alpha_{i\,-1}^{\delta} \quad \alpha_{i\,0}^{\delta} \quad \alpha_{i\,1}^{\delta} \quad \cdots \quad \alpha_{i\,m}^{\delta} \quad \alpha_{i\,m+1}^{\delta}\right]^T \tag{25}$$

Mapping

A generic cubic isoparametric spline finite strip is illustrated in Fig.4. Fig. 4(a) shows its representation in the local Cartesian coordinate system while Fig. 4(b) shows its mapping into the curvilinear coordinate system.

Dealing with plane strips, the position of the generic point of the mid-surface is simply defined by the Cartesian coordinates x and y. They are expressed in terms of the curvilinear coordinates ξ and η by

$$x(\xi,\eta) = \sum_{i=1}^{4}\sum_{j=-1}^{m+1} L_i(\xi)\phi_j(\eta)\bar{\beta}_{ij}^{x} \tag{26}$$

$$y(\xi,\eta) = \sum_{i=1}^{4}\sum_{j=-1}^{m+1} L_i(\xi)\phi_j(\eta)\bar{\beta}_{ij}^{y} \tag{27}$$

where $\bar{\beta}_{ij}^{x}$ and $\bar{\beta}_{ij}^{y}$ are numerical coefficients to be determined from the geometry. They comprise $4(m+3)$ coefficients for each coordinate.

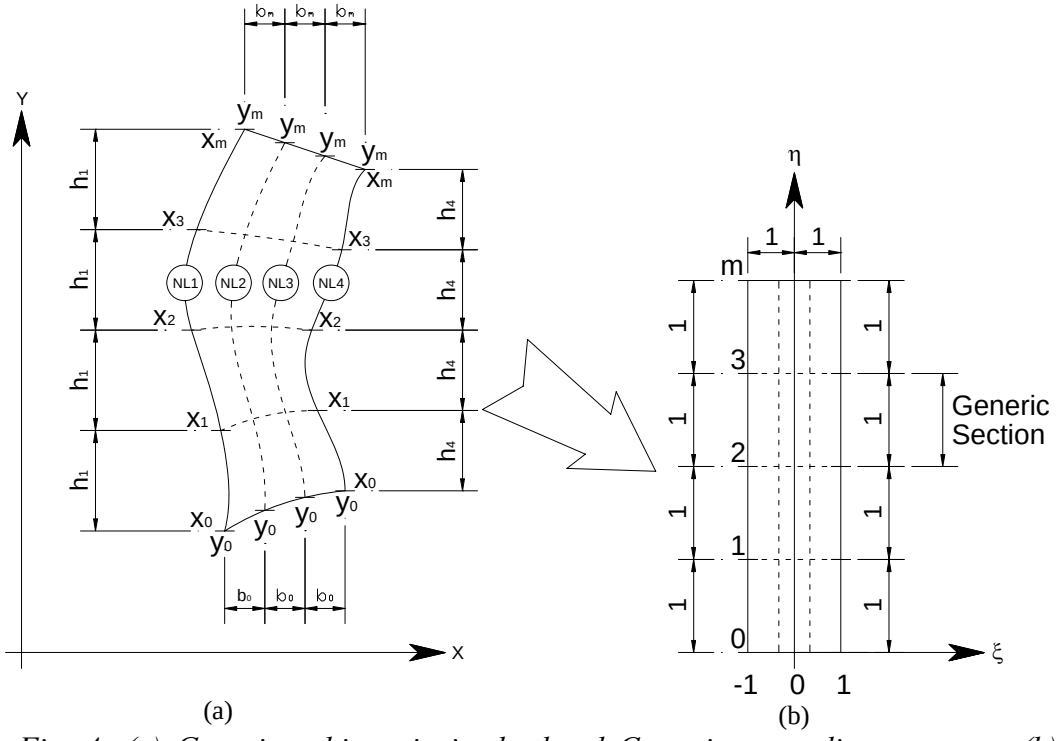

Fig. 4: (a) Generic cubic strip in the local Cartesian coordinate system; (b) Generic strip mapped into the curvilinear coordinate system

As shown in [1], the number of geometrical coefficients can be reduced to those lying on the perimeter of the strip by using an appropriate pre-determined choice of the location of the internal nodes. (26) and (27) can be rewritten as

$$x(\xi,\eta)=\sum_{j=-1}^{m_s+1}\phi_j(\eta)\left(\overline{\beta}_{1j}^{x}+\frac{\overline{\beta}_{4j}^{x}-\overline{\beta}_{1j}^{x}}{2}(\xi+1)\right) \tag{28}$$

$$y(\xi,\eta)=\sum_{\mathrm{i}=1}^{4}L_i(\xi)\left(y_{i0}+\frac{y_{im}-y_{i0}}{m_s}\eta\right) \tag{29}$$

where the coefficients $\overline{\beta}_{1j}^{x}$ and $\overline{\beta}_{4j}^{x}$ refer to the first and forth nodal line only, i.e. the external nodal lines, and y_{i0} and y_{im} are the *y*-coordinates of the starting and ending nodes, respectively, of each nodal line.

Taking the derivatives of (28) and (29), the components of the Jacobian matrix, **J**, of the transformation can be expressed by

$$\begin{bmatrix}\frac{\partial\xi}{\partial x} & \frac{\partial\eta}{\partial x}\\ \frac{\partial\xi}{\partial y} & \frac{\partial\eta}{\partial y}\end{bmatrix}=\begin{bmatrix}\frac{\partial x}{\partial\xi} & \frac{\partial y}{\partial\xi}\\ \frac{\partial x}{\partial\eta} & \frac{\partial y}{\partial\eta}\end{bmatrix}^{-1}=\mathbf{J}^{-\mathrm{T}} \tag{30}$$

where

$$\frac{\partial x(\xi,\eta)}{\partial\xi}=\sum_{j=-1}^{m+1}\left(\phi_j(\eta)\cdot\frac{\overline{\beta}_{4j}^{x}-\overline{\beta}_{1j}^{x}}{2}\right) \tag{31}$$

$$\frac{\partial x(\xi,\eta)}{\partial\eta}=\sum_{j=-1}^{m+1}\phi_j'(\eta)\left(\overline{\beta}_{1j}^{x}+\frac{\overline{\beta}_{4j}^{x}-\overline{\beta}_{1j}^{x}}{2}(\xi+1)\right) \tag{32}$$

$$\frac{\partial y(\xi,\eta)}{\partial\xi}=\sum_{\mathrm{i}=1}^{4}L_i'(\xi)\left(y_{i0}+\frac{y_{im}-y_{i0}}{m}\eta\right) \tag{33}$$

$$\frac{\partial y(\xi,\eta)}{\partial\eta}=\sum_{\mathrm{i}=1}^{4}\left(L_i(\xi)\cdot\frac{y_{im}-y_{i0}}{m}\right) \tag{34}$$

where the prime symbol on the shape functions indicates the total derivative, i.e.

$$L_i'(\xi)=\frac{dL_i(\xi)}{d\xi} \tag{35}$$

$$\phi_j'(\eta)=\frac{d\phi_j(\eta)}{d\eta} \tag{36}$$

Kinematics assumptions and displacement functions

The kinematics field at a generic point, P, within a plate can be represented by the displacement along the transverse local *x*-coordinate, u_p, the displacement along the longitudinal local *y*-coordinate, v_p, and the out-of-plane displacement along the local *z*-coordinate, w_p. According to the assumption shown in Fig. 1, the displacement field at the generic point can be expressed by means of the out-of-plane displacement, *w*, and the rotations, θ_x and θ_y, of the mid-surface, i.e.

$$u_p = z\theta_x \tag{37}$$

$$v_p = z\theta_y \tag{38}$$

$$w_p = w \tag{39}$$

The mid-surface rotations, θ_x and θ_y, are defined so as to produce positive values of the displacements u_p and v_p on the positive portion of the *z*-axis, for positive rotations. The mid-surface displacement, *w*, and rotations, θ_x and θ_y, are expressed in terms of displacement functions, L_i and ϕ_j, and generalised displacements, α_{ij}^{δ}, as

$$w(\xi,\eta) = \sum_{i=1}^{4}\sum_{j=-1}^{m_s+1} L_i(\xi)\,\phi_j(\eta)\,\alpha_{ij}^{w} \tag{40}$$

$$\theta_x(\xi,\eta) = \sum_{i=1}^{4}\sum_{j=-1}^{m_s+1} L_i(\xi)\,\phi_j(\eta)\,\alpha_{ij}^{\theta_x} \tag{41}$$

$$\theta_y(\xi,\eta) = \sum_{i=1}^{4}\sum_{j=-1}^{m_s+1} L_i(\xi)\,\phi_j(\eta)\,\alpha_{ij}^{\theta_y} \tag{42}$$

It is convenient to present the matrix formulation for the flexural displacement field, $\mathbf{u}_b$

$$\mathbf{u}_b = \mathbf{N}_b\,\boldsymbol{\alpha}_b \tag{43}$$

where

$$\mathbf{u}_b = \mathbf{u}_b(\xi,\eta) = \begin{bmatrix} w(\xi,\eta) \\ \theta_x(\xi,\eta) \\ \theta_y(\xi,\eta) \end{bmatrix} \tag{44}$$

$$\mathbf{N}_b = \begin{bmatrix} \mathbf{N}_1 & 0 & 0 & \mathbf{N}_2 & 0 & 0 & \mathbf{N}_3 & 0 & 0 & \mathbf{N}_4 & 0 & 0 \\ 0 & \mathbf{N}_1 & 0 & 0 & \mathbf{N}_2 & 0 & 0 & \mathbf{N}_3 & 0 & 0 & \mathbf{N}_4 & 0 \\ 0 & 0 & \mathbf{N}_1 & 0 & 0 & \mathbf{N}_2 & 0 & 0 & \mathbf{N}_3 & 0 & 0 & \mathbf{N}_4 \end{bmatrix} \tag{45}$$

$$\boldsymbol{\alpha}_b = \begin{bmatrix} \boldsymbol{\alpha}_1^{wT} & \boldsymbol{\alpha}_1^{\theta_x T} & \boldsymbol{\alpha}_1^{\theta_y T} & \boldsymbol{\alpha}_2^{wT} & \boldsymbol{\alpha}_2^{\theta_x T} & \boldsymbol{\alpha}_2^{\theta_y T} & \boldsymbol{\alpha}_3^{wT} & \boldsymbol{\alpha}_3^{\theta_x T} & \boldsymbol{\alpha}_3^{\theta_y T} & \boldsymbol{\alpha}_4^{wT} & \boldsymbol{\alpha}_4^{\theta_x T} & \boldsymbol{\alpha}_4^{\theta_y T} \end{bmatrix}^T \tag{46}$$

$\mathbf{N}_i$ represents the i^{th} displacement function and $\boldsymbol{\alpha}_i^{\delta}$ the spline nodal coefficients referring to the i^{th} nodal line and the general displacement function, δ.

Strain-displacement relations

The relevant strains in plate bending according to the Mindlin theory are those given in (3)-(7). It is convenient to separate the plate bending strains into the flexural strains, $\boldsymbol{\varepsilon}_f$, and the shear strains, $\boldsymbol{\varepsilon}_s$, defined as

$$\boldsymbol{\varepsilon}_f = \begin{Bmatrix} \chi_{xx} \\ \chi_{yy} \\ \chi_{xy} \end{Bmatrix} = \begin{Bmatrix} \dfrac{\partial \theta_x}{\partial x} \\ \dfrac{\partial \theta_y}{\partial y} \\ \dfrac{\partial \theta_x}{\partial y} + \dfrac{\partial \theta_y}{\partial x} \end{Bmatrix} \tag{47}$$

$$\boldsymbol{\varepsilon}_s = \begin{Bmatrix} \gamma_{xz} \\ \gamma_{yz} \end{Bmatrix} = \begin{Bmatrix} \dfrac{\partial w}{\partial x} + \theta_x \\ \dfrac{\partial w}{\partial y} + \theta_y \end{Bmatrix} \tag{48}$$

The derivatives that appear in (47) and in (48) refer to the local coordinate system, while the displacement functions, given in (40), (41) and (42) are expressed in natural coordinates, ξ and η. Following the chain rule, the linear strain-displacement relationship is obtained as

$$\boldsymbol{\varepsilon}_f = \begin{Bmatrix} \chi_{xx} \\ \chi_{yy} \\ \chi_{xy} \end{Bmatrix} = \begin{Bmatrix} \dfrac{\partial \theta_x}{\partial \xi}\dfrac{\partial \xi}{\partial x} + \dfrac{\partial \theta_x}{\partial \eta}\dfrac{\partial \eta}{\partial x} \\ \dfrac{\partial \theta_y}{\partial \xi}\dfrac{\partial \xi}{\partial y} + \dfrac{\partial \theta_y}{\partial \eta}\dfrac{\partial \eta}{\partial y} \\ \left(\dfrac{\partial \theta_x}{\partial \xi}\dfrac{\partial \xi}{\partial y} + \dfrac{\partial \theta_x}{\partial \eta}\dfrac{\partial \eta}{\partial y}\right) + \left(\dfrac{\partial \theta_y}{\partial \xi}\dfrac{\partial \xi}{\partial x} + \dfrac{\partial \theta_y}{\partial \eta}\dfrac{\partial \eta}{\partial x}\right) \end{Bmatrix} \tag{49}$$

$$\boldsymbol{\varepsilon}_s = \begin{Bmatrix} \gamma_{xz} \\ \gamma_{yz} \end{Bmatrix} = \begin{Bmatrix} \left(\dfrac{\partial w}{\partial \xi}\dfrac{\partial \xi}{\partial x} + \dfrac{\partial w}{\partial \eta}\dfrac{\partial \eta}{\partial x} \right) + \theta_x \\ \left(\dfrac{\partial w}{\partial \xi}\dfrac{\partial \xi}{\partial y} + \dfrac{\partial w}{\partial \eta}\dfrac{\partial \eta}{\partial y} \right) + \theta_y \end{Bmatrix} \tag{50}$$

Introducing the general displacement, δ, we have

$$\frac{\partial \delta}{\partial \xi} = \sum_{i=1}^{4}\sum_{j=-1}^{m_s+1} L_i'(\xi)\,\phi_j(\eta)\,\alpha_{ij}^{\delta} \;; \quad (\delta = w, \theta_x, \theta_y) \tag{51}$$

$$\frac{\partial \delta}{\partial \eta} = \sum_{i=1}^{4}\sum_{j=-1}^{m_s+1} L_i(\xi)\,\phi_j'(\eta)\,\alpha_{ij}^{\delta} \;; \quad (\delta = w, \theta_x, \theta_y) \tag{52}$$

where

$$L_i'(\xi) = \frac{dL_i(\xi)}{d\xi} \tag{53}$$

$$\phi_j'(\eta) = \frac{d\phi_j(\eta)}{d\eta} \tag{54}$$

while the quantities $\dfrac{\partial \xi}{\partial x}, \dfrac{\partial \eta}{\partial x}, \dfrac{\partial \xi}{\partial y}$ and $\dfrac{\partial \eta}{\partial y}$ can be obtained from (31) to (34).

It is convenient to express (49) and (50) in terms of the strain matrices, $\mathbf{B}_f$ and $\mathbf{B}_s$, and the vector, $\boldsymbol{\alpha}_b$, containing the generalised displacements for the bending problem,

$$\boldsymbol{\varepsilon}_f = \mathbf{B}_f\,\boldsymbol{\alpha}_b \tag{55}$$

$$\boldsymbol{\varepsilon}_s = \mathbf{B}_s\,\boldsymbol{\alpha}_b \tag{56}$$

where

$$\mathbf{B}_f = \begin{bmatrix} 0 & \mathbf{B}_{1,x} & 0 & 0 & \mathbf{B}_{2,x} & 0 & 0 & \mathbf{B}_{3,x} & 0 & 0 & \mathbf{B}_{4,x} & 0 \\ 0 & 0 & \mathbf{B}_{1,y} & 0 & 0 & \mathbf{B}_{2,y} & 0 & 0 & \mathbf{B}_{3,y} & 0 & 0 & \mathbf{B}_{4,y} \\ 0 & \mathbf{B}_{1,y} & \mathbf{B}_{1,x} & 0 & \mathbf{B}_{2,y} & \mathbf{B}_{2,x} & 0 & \mathbf{B}_{3,y} & \mathbf{B}_{3,x} & 0 & \mathbf{B}_{4,y} & \mathbf{B}_{4,x} \end{bmatrix} \tag{57}$$

$$\mathbf{B}_s = \begin{bmatrix} \mathbf{B}_{1,x} & \mathbf{N}_1 & 0 & \mathbf{B}_{2,x} & \mathbf{N}_2 & 0 & \mathbf{B}_{3,x} & \mathbf{N}_3 & 0 & \mathbf{B}_{4,x} & \mathbf{N}_4 & 0 \\ \mathbf{B}_{1,y} & 0 & \mathbf{N}_1 & \mathbf{B}_{2,y} & 0 & \mathbf{N}_2 & \mathbf{B}_{3,y} & 0 & \mathbf{N}_3 & \mathbf{B}_{4,y} & 0 & \mathbf{N}_4 \end{bmatrix} \tag{58}$$

where the j^{th} component of the row matrices $\mathbf{B}_{i,x}$ and $\mathbf{B}_{i,y}$ is given by

$$\left(\mathbf{B}_{i,x}\right)_j = L_i'(\xi)\,\phi_j(\eta)\frac{\partial \xi}{\partial x} + L_i(\xi)\,\phi_j'(\eta)\frac{\partial \eta}{\partial x} \tag{59}$$

$$\left(\mathbf{B}_{i,y}\right)_j = L_i'(\xi)\,\phi_j(\eta)\frac{\partial \xi}{\partial y} + L_i(\xi)\,\phi_j'(\eta)\frac{\partial \eta}{\partial y} \tag{60}$$

and the general shape function row matrix, $\mathbf{N}_i$, is given in (24).

Stress-strain relations

The stress state may be described by the resultant of the stresses integrated over the thickness. The resultants per unit width relevant to the flexural deformations are given by the transverse bending moment, m_{xx}, the longitudinal bending moment, m_{yy}, and the twisting bending moment, m_{xy}. According to the kinematics assumptions made for plate bending according to the Mindlin theory, the out-of-plane shear stresses are constant within the thickness of the plate and can be alternatively represented by the shear stress values, τ_{xz} and τ_{xy}, or by the resultants integrated over the thickness, s_{xz} and s_{yz}. To be consistent with the expression for the in-plane shear stress, τ_{xy}, used in the plane stress state analysis, we use here the shear stress values, τ_{xz} and τ_{yz}.

According to the linear elastic theory, the relation between stresses and strains is given through the constant constitutive matrices, $\mathbf{D}_f$ and $\mathbf{D}_s$, i.e.

$$\boldsymbol{\sigma}_f = \mathbf{D}_f\,\boldsymbol{\varepsilon}_f = \mathbf{D}_f\,\mathbf{B}_f\,\boldsymbol{\alpha}_b \tag{61}$$

$$\boldsymbol{\sigma}_s = \mathbf{D}_s\,\boldsymbol{\varepsilon}_s = \mathbf{D}_s\,\mathbf{B}_s\,\boldsymbol{\alpha}_b \tag{62}$$

where

$$\boldsymbol{\sigma}_f = \begin{bmatrix} m_{xx} & m_{yy} & m_{xy} \end{bmatrix}^T \tag{63}$$

$$\boldsymbol{\sigma}_s = \begin{bmatrix} \tau_{xz} & \tau_{yz} \end{bmatrix}^T \tag{64}$$

For an isotropic material with elastic modulus, E, and Poisson's ratio, ν, the constitutive matrices become

$$\mathbf{D}_f = \frac{Et^3}{12\left(1-\nu^2\right)}\begin{bmatrix} 1 & \nu & 0 \\ \nu & 1 & 0 \\ 0 & 0 & \frac{1}{2}(1-\nu) \end{bmatrix} \tag{65}$$

$$\mathbf{D}_s = \frac{E}{2.4(1+\nu)}\begin{bmatrix} 1 & 0 \\ 0 & 1 \end{bmatrix} \tag{66}$$

while for an orthotropic material, characterised by a transverse elastic modulus and Poisson ratio, E_x and ν_x, a longitudinal elastic modulus and Poisson ratio, E_y and ν_y, and by shear moduli, G_{xy}, G_{xz}, and G_{yz}, the constitutive matrix becomes

$$\mathbf{D}_f = \frac{t^3}{12}\begin{bmatrix} \dfrac{E_x}{1-\nu_x\nu_y} & \dfrac{\nu_y E_x}{1-\nu_x\nu_y} & 0 \\ \dfrac{\nu_x E_y}{1-\nu_x\nu_y} & \dfrac{E_y}{1-\nu_x\nu_y} & 0 \\ 0 & 0 & G_{xy} \end{bmatrix} \tag{67}$$

$$\mathbf{D}_s = \frac{1}{1.2}\begin{bmatrix} G_{xz} & 0 \\ 0 & G_{yz} \end{bmatrix} \tag{68}$$

Equilibrium equation

The equilibrium condition of the finite strip system is given according to the principle of virtual displacements, or by the equivalent principle of stationarity of the total potential energy of the system.

For plate bending, the elastic potential strain energy of the strip, U_b^s, is expressed by

$$\begin{aligned} U_b^s &= U_f^s + U_s^s = \frac{1}{2}\int_V \boldsymbol{\sigma}_f{}^T\, \boldsymbol{\varepsilon}_f\, dV + \frac{1}{2}\int_V \boldsymbol{\sigma}_s{}^T\, \boldsymbol{\varepsilon}_s\, dV \\ &= \frac{1}{2}t\int_A \boldsymbol{\sigma}_f{}^T\, \boldsymbol{\varepsilon}_f\, dA + \frac{1}{2}t\int_A \boldsymbol{\sigma}_s{}^T\, \boldsymbol{\varepsilon}_s\, dA \\ &= \frac{1}{2}t\int_{-1}^{1}\int_0^{m_s} \boldsymbol{\sigma}_f{}^T\, \boldsymbol{\varepsilon}_f\, \det(\mathbf{J})\, d\eta\, d\xi + \frac{1}{2}t\int_{-1}^{1}\int_0^{m_s} \boldsymbol{\sigma}_s{}^T\, \boldsymbol{\varepsilon}_s\, \det(\mathbf{J})\, d\eta\, d\xi \\ &= \frac{1}{2}\boldsymbol{\alpha}_b{}^T\left(t\int_{-1}^{1}\int_0^{m_s} \mathbf{B}_f{}^T\, \mathbf{D}_f\, \mathbf{B}_f\, \det(\mathbf{J})\, d\eta\, d\xi + t\int_{-1}^{1}\int_0^{m_s} \mathbf{B}_s{}^T\, \mathbf{D}_s\, \mathbf{B}_s\, \det(\mathbf{J})\, d\eta\, d\xi \right)\boldsymbol{\alpha}_b \\ &= \frac{1}{2}\boldsymbol{\alpha}_b{}^T\left(\mathbf{K}_f^s + \mathbf{K}_s^s\right)\boldsymbol{\alpha}_b \\ &= \frac{1}{2}\boldsymbol{\alpha}_b{}^T\,\mathbf{K}_b^s\,\boldsymbol{\alpha}_b \end{aligned} \tag{69}$$

where the single strip stiffness matrices, $\mathbf{K}_f^s$ and $\mathbf{K}_s^s$, are defined as

$$\mathbf{K}_f^s = t\int_{-1}^{1}\int_{0}^{m_s} \mathbf{B}_f{}^T\, \mathbf{D}_f\, \mathbf{B}_f \det(\mathbf{J})\, d\eta\, d\xi \tag{70}$$

$$\mathbf{K}_s^s = t\int_{-1}^{1}\int_{0}^{m_s} \mathbf{B}_s{}^T\, \mathbf{D}_s\, \mathbf{B}_s \det(\mathbf{J})\, d\eta\, d\xi \tag{71}$$

and t is the thickness which is assumed to be constant within the strip. As described in [12], Mindlin plate bending theory is prone to shear locking when the thickness of the plate becomes small. In order to enhance the performance of the finite strip formulation, a reduced Gaussian integration is performed on the shear stiffness matrix, $\mathbf{K}_s^s$, while full Gaussian integration is performed on the flexural stiffness matrix, $\mathbf{K}_f^s$.

The general expression for the potential energy of the external loads, V_b^s, is given by

$$\begin{aligned} V_b^s &= \int_V \mathbf{u}_b{}^T\, \mathbf{p}\, dV = t\int_A \mathbf{u}_b{}^T\, \mathbf{p}\, dA = t\int_{-1}^{1}\int_{0}^{m_s} \mathbf{u}_b{}^T\, \mathbf{p} \det(\mathbf{J})\, d\eta\, d\xi \\ &= \boldsymbol{\alpha}_b{}^T \left(t\int_{-1}^{1}\int_{0}^{m_s} \mathbf{N}_b{}^T\, \mathbf{p} \det(\mathbf{J})\, d\eta\, d\xi \right) \\ &= \boldsymbol{\alpha}_b{}^T\, \mathbf{v}_b^s \end{aligned} \tag{72}$$

where the vector **p** contains the external body force components along the different displacement functions, i.e.

$$\mathbf{p} = \mathbf{p}(\xi,\eta) = \begin{Bmatrix} p_z \\ p_{\theta_x} \\ p_{\theta_y} \end{Bmatrix} \tag{73}$$

while the equivalent strip force vector is defined as

$$\mathbf{v}_b^s = t\int_{-1}^{1}\int_{0}^{m_s} \mathbf{N}_b{}^T\, \mathbf{p} \det(\mathbf{J})\, d\eta\, d\xi \tag{74}$$

This general definition for $\mathbf{v}_b^s$ can be specialised to the different load types, i.e. body, surface, line and point loads. Introducing **b** for the equivalent force vector when **p** refers to body loads, the integration provides

$$\mathbf{b} = t\int_{-1}^{1}\int_{0}^{m_s} \mathbf{N}_b{}^T\, \mathbf{p}\, \det(\mathbf{J})\, d\eta\, d\xi \tag{75}$$

If we consider surface tractions, the equivalent load vector, **s**, is,

$$\mathbf{s} = \int_{-1}^{1}\int_{0}^{m_s} \mathbf{N}_b{}^T\, \mathbf{p}\, \det(\mathbf{J})\, d\eta\, d\xi \tag{76}$$

while for line loads along the natural coordinate ξ at given $\eta = \overline{\eta}$, we obtain the vector $\mathbf{l}_\xi$ as,

$$\mathbf{p} = \mathbf{p}(\xi, \overline{\eta}) = \begin{Bmatrix} p_z(\xi, \overline{\eta}) \\ p_{\theta_x}(\xi, \overline{\eta}) \\ p_{\theta_y}(\xi, \overline{\eta}) \end{Bmatrix} \tag{77}$$

$$\mathbf{l}_\xi = \int_{-1}^{1} \mathbf{N}_b{}^T\, \mathbf{p}\, ds_\xi\, d\xi \tag{78}$$

where

$$ds_\xi = ds_\xi(\xi, \overline{\eta}) = \sqrt{\left(\frac{\partial x(\xi, \overline{\eta})}{\partial \xi}\right)^2 + \left(\frac{\partial y(\xi, \overline{\eta})}{\partial \xi}\right)^2} \tag{79}$$

A line load developing along the natural coordinate η at given $\xi = \overline{\xi}$ can be expressed as $\mathbf{l}_\eta$,

$$\mathbf{p} = \mathbf{p}(\overline{\xi}, \eta) = \begin{Bmatrix} p_z(\overline{\xi}, \eta) \\ p_{\theta_x}(\overline{\xi}, \eta) \\ p_{\theta_y}(\overline{\xi}, \eta) \end{Bmatrix} \tag{80}$$

$$\mathbf{l}_\eta = \int_{0}^{m_s} \mathbf{N}_b{}^T\, \mathbf{p}\, ds_\eta\, d\eta \tag{81}$$

where

$$ds_\eta = ds_\eta\left(\bar{\xi},\eta\right) = \sqrt{\left(\frac{\partial x\left(\bar{\xi},\eta\right)}{\partial \eta}\right)^2 + \left(\frac{\partial y\left(\bar{\xi},\eta\right)}{\partial \eta}\right)^2} \tag{82}$$

In the case of a point load, where the integration reduces to the evaluation of the integrating functions at the point of loading $\left(\bar{\xi},\bar{\eta}\right)$, the equivalent force vector, **c**, becomes,

$$\mathbf{p} = \mathbf{p}\left(\bar{\xi},\bar{\eta}\right) = \begin{Bmatrix} p_z\left(\bar{\xi},\bar{\eta}\right) \\ p_{\theta_x}\left(\bar{\xi},\bar{\eta}\right) \\ p_{\theta_y}\left(\bar{\xi},\bar{\eta}\right) \end{Bmatrix} \tag{83}$$

$$\mathbf{c} = \mathbf{N}_b{}^T\left(\bar{\xi},\bar{\eta}\right)\mathbf{p}\left(\bar{\xi},\bar{\eta}\right) \tag{84}$$

Finally, we may express the total equivalent strip force vector as the summation of the contributions of the different load types, i.e.

$$\mathbf{v}_b^s = \mathbf{b} + \mathbf{s} + \mathbf{l}_\xi + \mathbf{l}_\eta + \mathbf{c} \tag{85}$$

The total potential energy of the strip is expressed by

$$\Pi_b^s = U_b^s + V_b^s \tag{86}$$

and can be rewritten in matrix form as

$$\Pi_b^s = \frac{1}{2}\boldsymbol{\alpha}_b{}^T\,\mathbf{K}_b^s\,\boldsymbol{\alpha}_b - \boldsymbol{\alpha}_b{}^T\,\mathbf{v}_b^s \tag{87}$$

The potential energy for the entire structure can be obtained by the well-known assembling process, which consists of adding the stiffness matrix, $\mathbf{K}_b^s$, and the load vector contributions, $\mathbf{v}_b^s$, of each strip into the global matrix, $\mathbf{K}_b$, and global vector, $\mathbf{v}_b$, respectively, to obtain the total potential energy of the structure, i.e.

$$\Pi_b = \frac{1}{2}\boldsymbol{\alpha}_b{}^T\,\mathbf{K}_b\,\boldsymbol{\alpha}_b - \boldsymbol{\alpha}_b{}^T\,\mathbf{v}_b \tag{88}$$

where

$$\mathbf{K}_b = \text{"}\sum \mathbf{K}_b^s\text{"} \tag{89}$$

$$\mathbf{v}_b = \text{"}\sum \mathbf{v}_b^s\text{"} \tag{90}$$

where the summations in (89) and (90) stand for the assembling process and $\boldsymbol{\alpha}_b$ now represents the unknown vector of spline nodal coefficients of the entire structure.

The equilibrium condition is finally given by $\delta\Pi = 0$ and provides a linear system in the unknown vector $\boldsymbol{\alpha}_b$, i.e.

$$\mathbf{K}_b\, \boldsymbol{\alpha}_b = \mathbf{v}_b \tag{91}$$

Examples of plate bending analysis

In the following examples, perforated plates are subjected to bending deformations applied by imposing rotations along a part of their transverse edges. The examples of square plates with elliptical, rectangular and diamond shaped perforations are presented. The results obtained with the isoparametric spline finite strip method are compared with results produced by a finite element analysis [13]. Eight-node quadratic shell elements have been used in the finite element method analysis.

Bending of a square plate with elliptical perforations

The geometry of the perforated plate is given in Fig. 5. The plate is simply supported in the out-of-plane direction along the perimeter. The transverse edges are restrained in the longitudinal direction, while the longitudinal edges are restrained in the transverse direction. The load is introduced by imposing a rotation to a portion of the transverse edges, as shown in Fig. 6 (a). The results obtained with the isoparametric spline finite strip method are compared with those obtained from an Abaqus finite element analysis. The finite strip and finite element meshes are shown in Fig. 7 and compared in Table 1. The results are compared in terms of displacements (deflection) and stresses at the top surface of the plate along the three reference axes defined in Fig. 6 (b), as shown in Fig. 8 to Fig. 13. Two different cases are considered: longitudinal pinned edges and longitudinal fixed edges. The solid lines are associated with the results obtained with the spline finite strip simulation, while the dashed lines refer to the results obtained with Abaqus. Fig. 8 (a) and Fig. 8 (b) show the contour plot of the plate deflection, where the effect of the longitudinal rotational restrains is clearly visible.

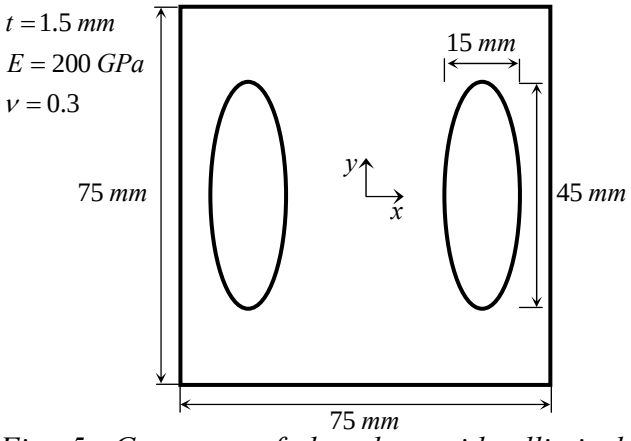

Fig. 5: Geometry of the plate with elliptical perforations.

The effect of the rotational restraints is quantified in Fig. 9 and Fig. 11. Rotational restrains reduce the deflection along the longitudinal symmetry axis by more than 20 percent. Similarly, the longitudinal stress component in the central part of the plate is reduced by more than 30 percent, as shown in Fig. 10 and Fig. 12.

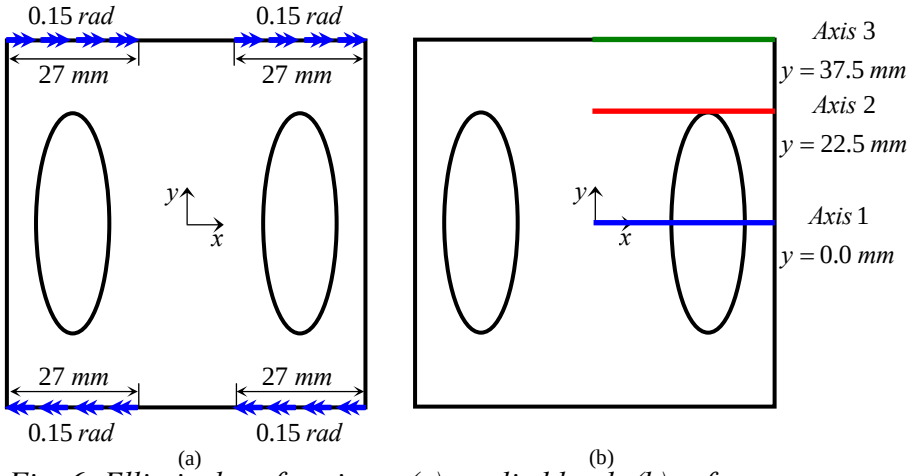

Fig. 6: Elliptical perforations: (a) applied load; (b) reference axes.

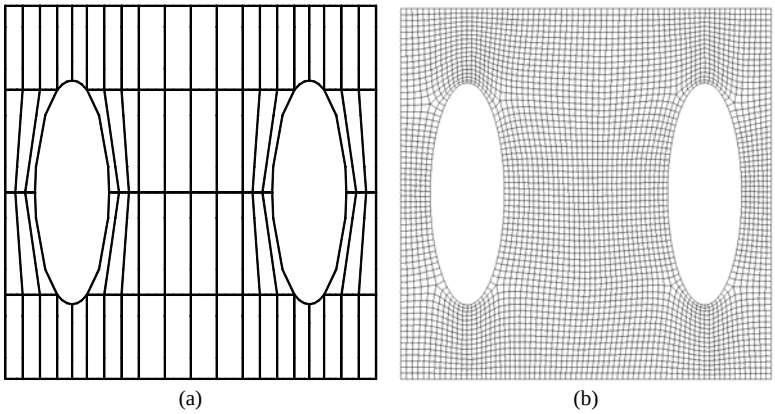

Fig. 7: Elliptical perforations: (a) isfsm mesh; (b) fem/abaqus mesh.

	Strips (Elements)	Nodes	Dofs
ISFSM	72	3116	15580
FEM/ABAQUS	3710	11581	69486
Ratio FEM/ISFSM	51.5	3.7	4.5

Table 1: Elliptical perforations, mesh comparison.

The deflection of the central part of the plate is almost constant for both boundary conditions, assuming a value of about 1.9 mm and 2.6 mm for fixed longitudinal edges and pinned longitudinal edges, respectively. The portion of the plate lying on the outer side of the perforation undergoes much smaller deformations, which are highly influenced by the longitudinal rotational constraints: a practically zero deformation is obtained in the case of fixed longitudinal edges while a nearly linearly varying deformation is obtained in the case of longitudinal pinned edges with a maximum deflection of 0.7 mm at the edge of the perforation, point C, as shown in Fig. 11.

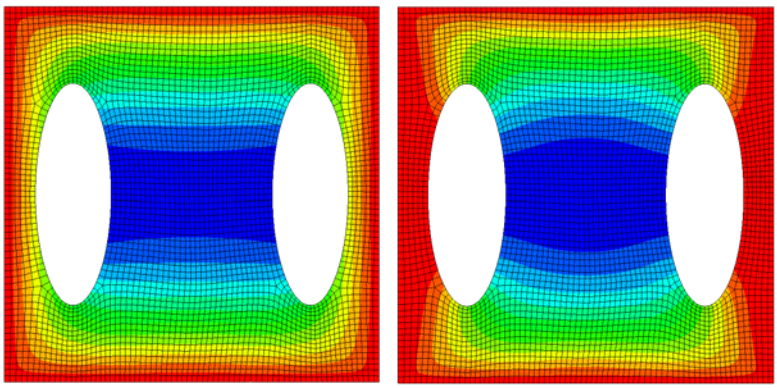

(a) (b)

Fig. 8: Elliptical perforations, deflection contour plot: (a) longitudinal pinned edges; (b) longitudinal fixed edges.

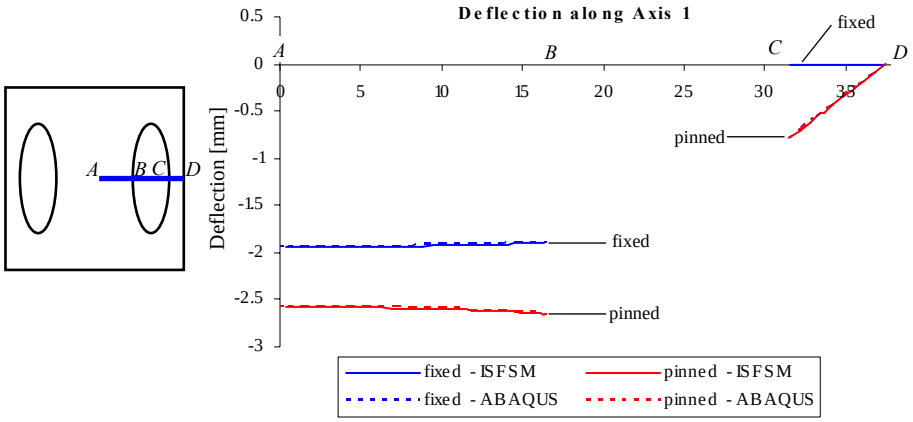

Fig. 9: Elliptical perforations, deflection comparison along axis 1.

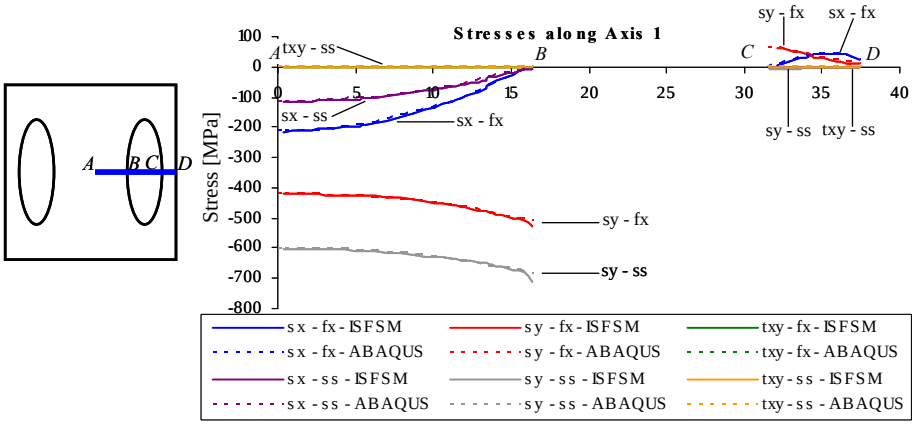

Fig. 10: Elliptical perforations, stress comparison along axis 1.

A very good agreement is obtained between the isoparametric spline finite strip analysis results and the finite element analysis result, both in terms of displacements and stresses. A maximum difference of about 3.5 percent is encountered for the stresses in the areas of high stress gradient, point *B* along axis 1, and is attributed to stress smoothing procedures, adopted in the Abaqus finite element analysis but not in the spline finite strip analysis.

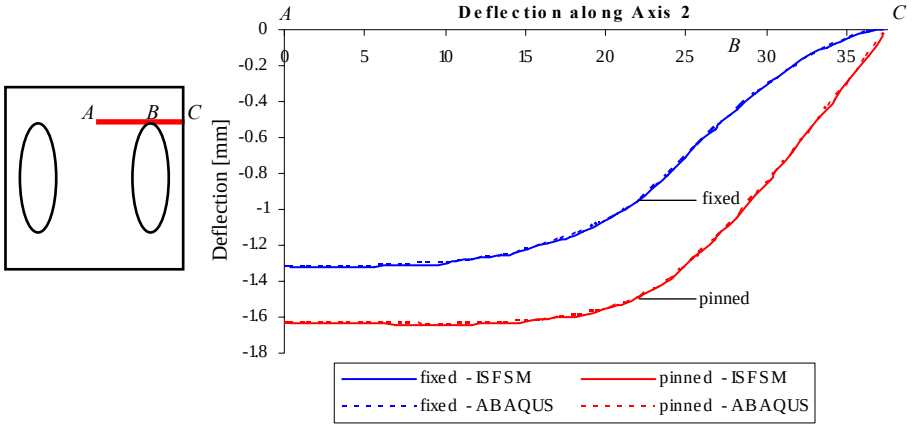

Fig. 11: Elliptical perforations, deflection comparison along axis 2.

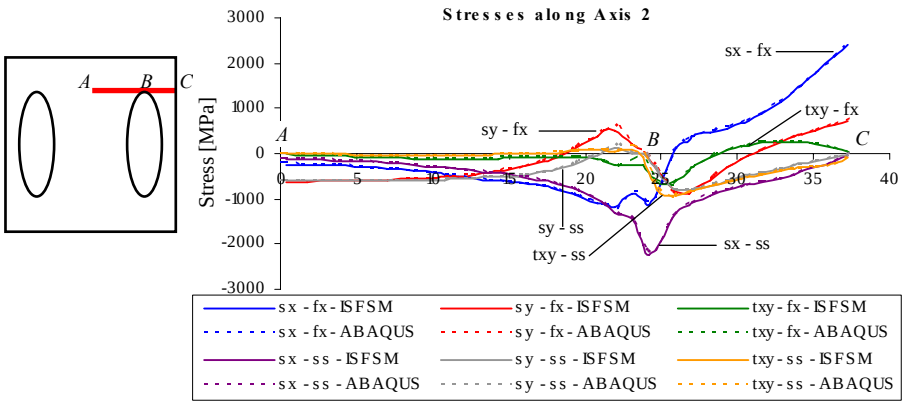

Fig. 12: Elliptical perforations, stress comparison along axis 2.

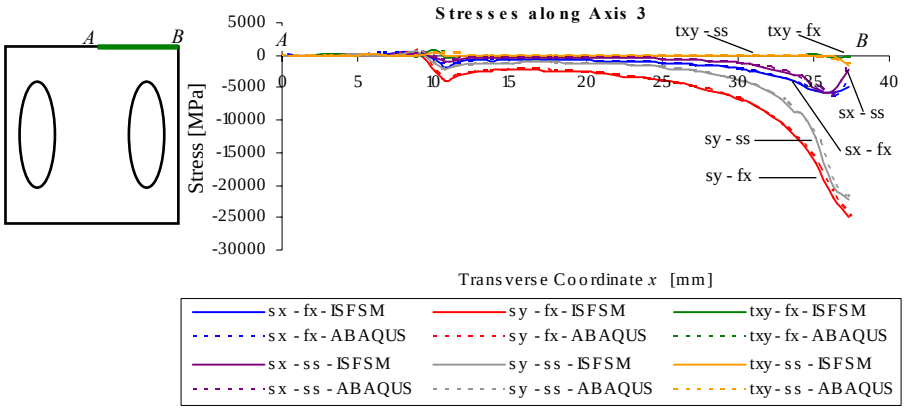

Fig. 13: Elliptical perforations, stress comparison along axis 3.

Bending of a square plate with rectangular perforations

The second example of plate bending concerns the square plate with two rectangular perforations shown in Fig. 14. The plate is supported and loaded in the same way as the plate with elliptical holes, as shown in Fig. 14 and Fig. 15. The results obtained with the isoparametric spline finite strip method are compared with those obtained with Abaqus along the three reference axes defined in Fig. 15 (b).

The meshes utilized are shown in Fig. 16 and Table 2. A contour plot of the out-of-plane deflection is shown in Fig. 17 while the comparison of the numerical results along the reference axes, in terms of both deflection and stresses at the top surface, is shown in Fig. 18 to Fig. 22.

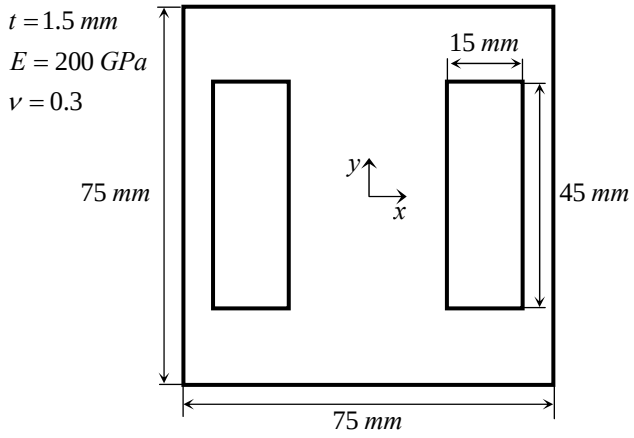

Fig. 14: Rectangular perforations, geometry of the problem.

The effect of the rotational restraints is to reduce the deflection of the longitudinal symmetry axis by more than 15 percent and the longitudinal stress component in the central part of the plate by approximately 20 percent, as shown in Fig. 18 and Fig. 19, respectively.

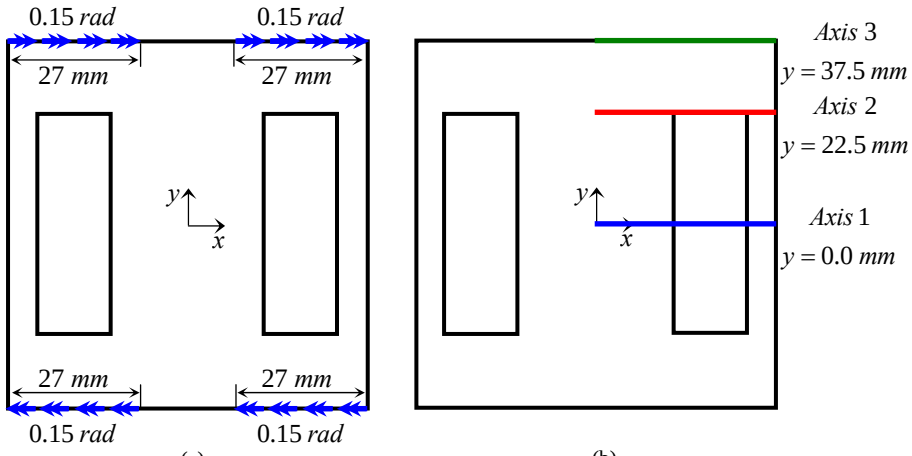

Fig. 15: Rectangular perforations: (a) applied load; (b) reference axis.

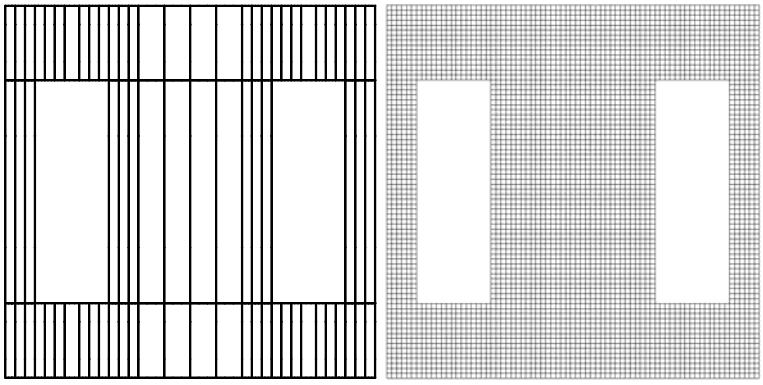

Fig. 16: Rectangular perforations: (a) Isfsm mesh; (b) Fem/Abaqus mesh.

	Strips (Elements)	Nodes	Dofs
ISFSM	76	3845	19225
FEM/ABAQUS	4275	13364	80184
Ratio FEM/ISFSM	56.3	3.5	4.2

Table 2: Rectangular perforations, mesh comparison.

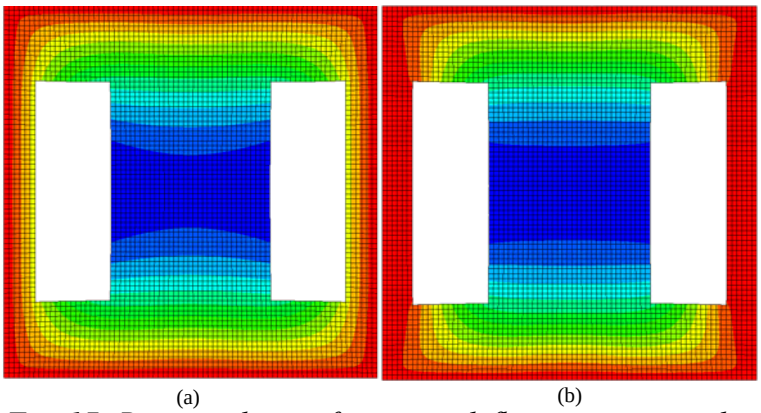

Fig. 17: Rectangular perforations, deflection contour plot: (a) longitudinal pinned edges; (b) longitudinal fixed edges.

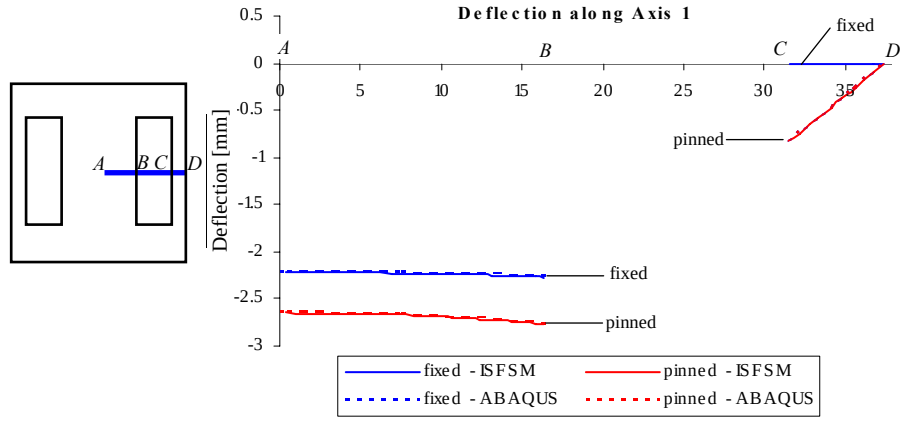

Fig. 18: Rectangular perforations, deflection comparison along axis 1.

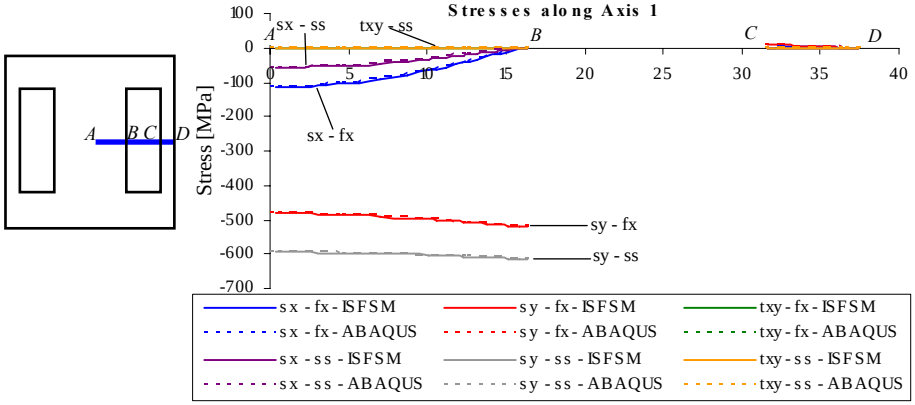

Fig. 19: Rectangular perforations, stress comparison along axis 1.

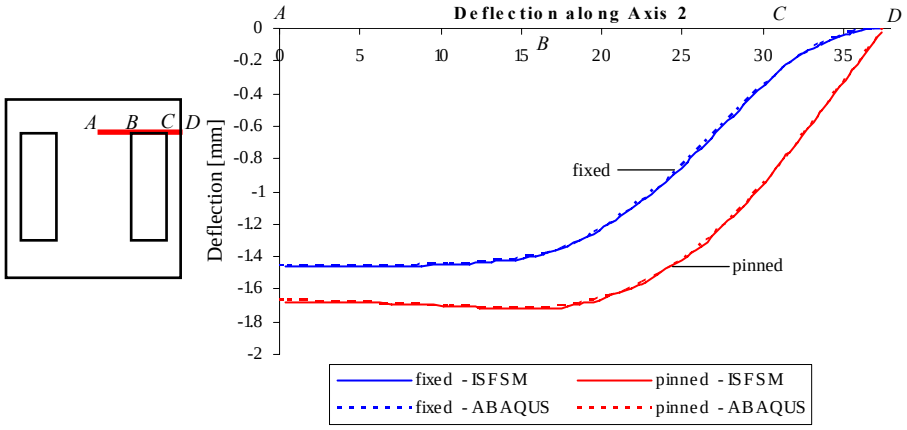

Fig. 20: Rectangular perforations, deflection comparison along axis 2.

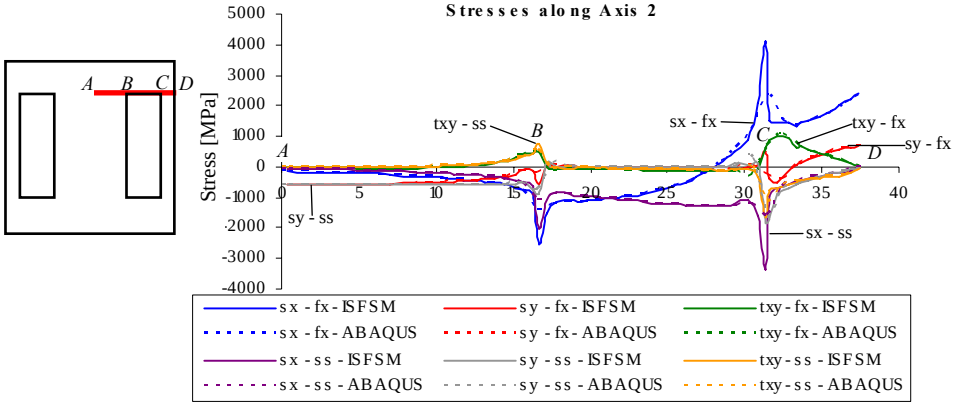

Fig. 21: Rectangular perforations, stress comparison along axis 2.

The deflection of the central part of the plate is almost constant for both longitudinal boundary conditions, assuming values of about 2.2 mm and 2.7 mm for fixed longitudinal edges and for pinned longitudinal edges, respectively, as shown in Fig. 18. These values are slightly higher than in the case of elliptical perforations.

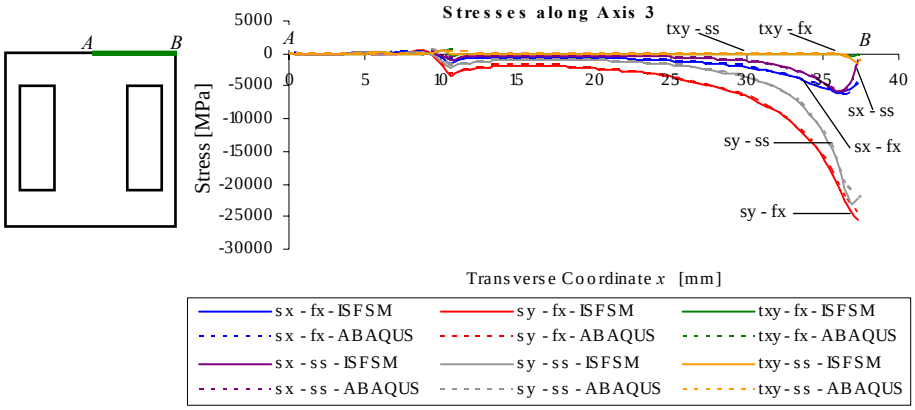

Fig. 22: Rectangular perforations, stress comparison along axis 3.

A very good agreement is obtained between the isoparametric spline finite strip analysis results and the finite element analysis results, both in terms of displacements and stresses. In the stress comparisons, the largest differences are encountered along axis 2, at the singular points *B* and *C*. Again, the discrepancy is attributed to the stress smoothing technique adopted in Abaqus.

Bending of a square plate with diamond perforations

The case of square plate with diamond perforations is presented next. The overall geometry of the problem is shown in Fig. 23. The support and loading conditions are the same as those considered for the plates with elliptical and rectangular holes, and the results are presented for three reference axes as shown in Fig. 24 (a) and Fig. 24 (b). The meshes utilized in the analyses are shown in Fig. 25 and Table 3.

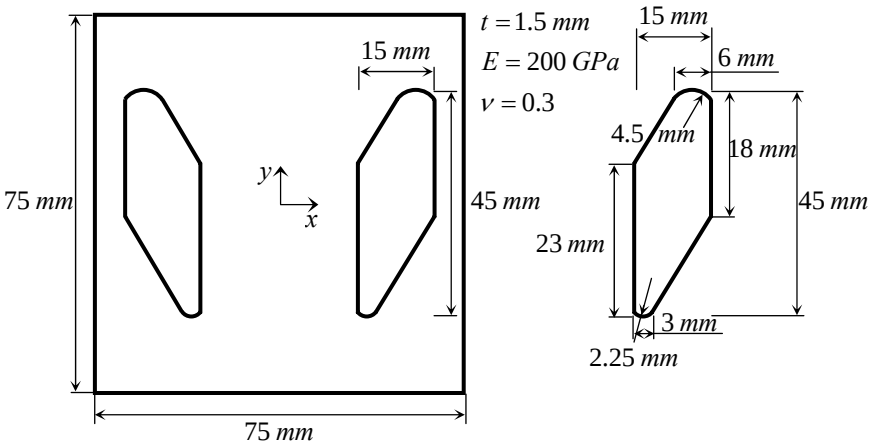

Fig. 23: Diamond perforations geometry.

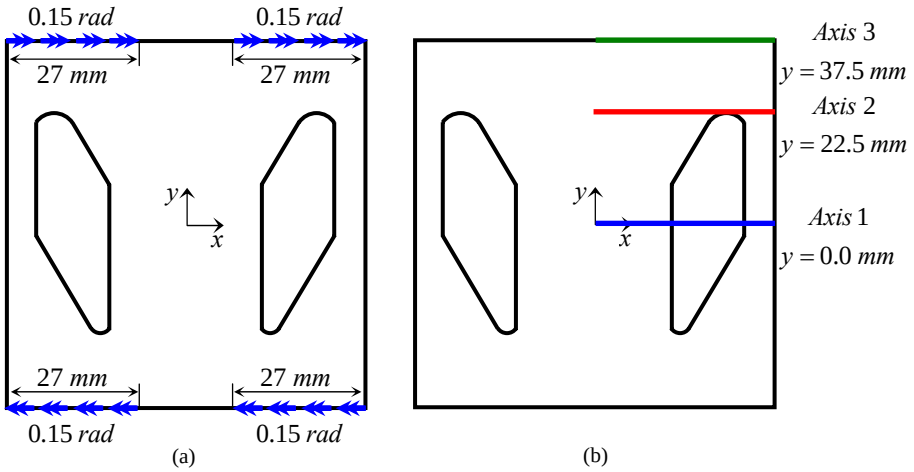

Fig. 24: Diamond perforations: (a) applied load; (b) reference axes.

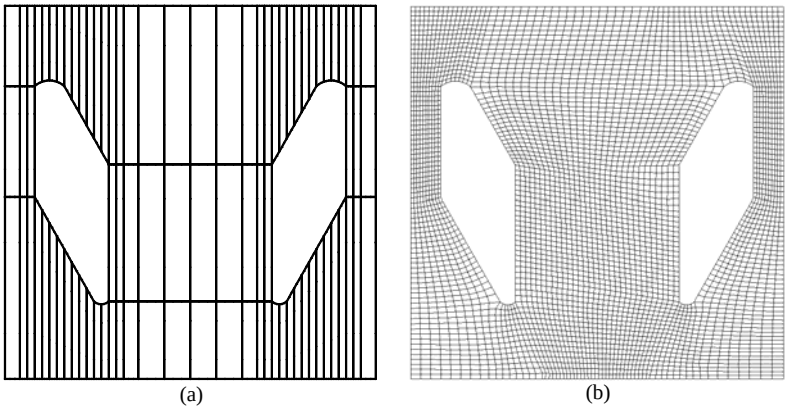

Fig. 25: Diamond perforations: (a) Isfsm mesh; (b) Fem/Abaqus mesh.

	Strips (Elements)	Nodes	Dofs
ISFSM	88	5473	27365
FEM/ABAQUS	4253	13234	79404
Ratio FEM/ISFSM	48.3	2.4	2.9

Table 3: Diamond perforations, mesh comparison.

The contour plots of the out-of-plane deflection are shown in Fig. 26 (a) and Fig. 26 (b), for the cases of pinned and fixed longitudinal edges, respectively.

The deflection curves along the reference axes are presented in Fig. 27 and Fig. 29, as obtained with the spline finite strip and finite element analyses. The stress comparison is shown in Fig. 28, Fig. 30 and Fig. 31.

The highest displacement and stress values are encountered in the central portion of the plate as shown in Fig. 27. An almost uniform deformation is induced in the central area in between the perforations, assuming the values of approximately 1.9 mm and 2.6 mm for fixed and pinned longitudinal edges,

respectively. The different rotational boundary conditions affect the deflection and top surface stresses along the vertical axis of symmetry by about 25 percent.

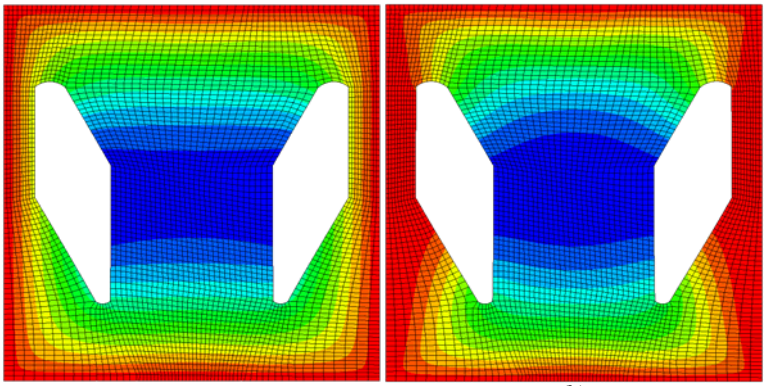

(a) (b)

Fig. 26: Diamond perforations, deflection contour plot: (a) longitudinal pinned edges; (b) longitudinal fixed edges.

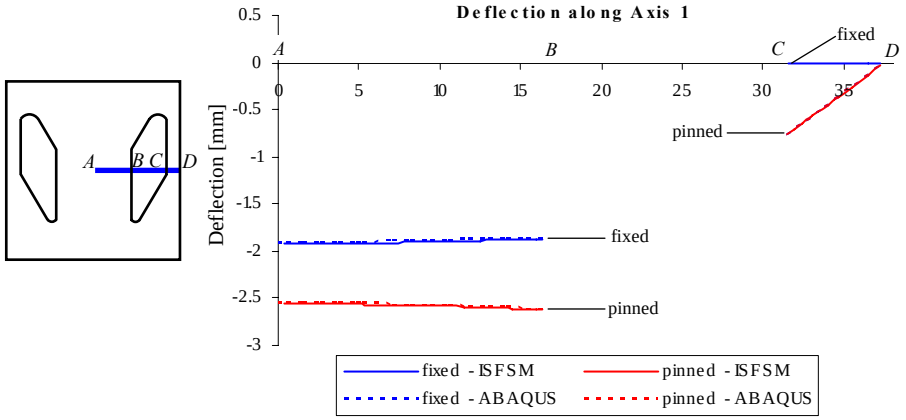

Fig. 27: Diamond perforations, deflection comparison along axis 1.

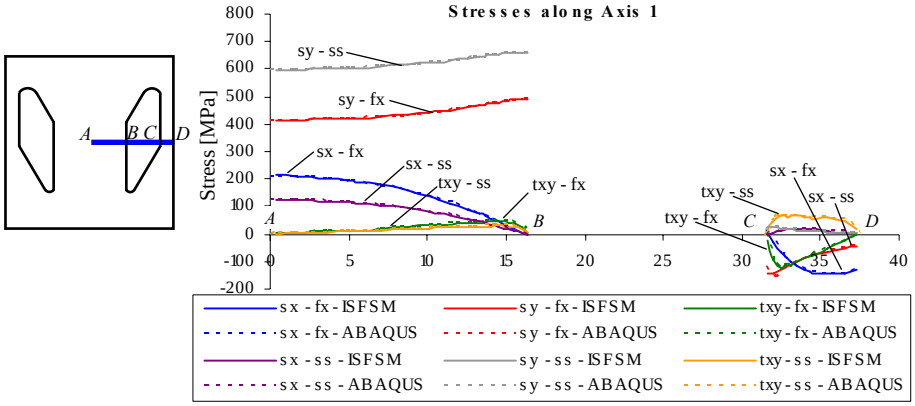

Fig. 28: Diamond perforations, stress comparison along axis 1.

Overall, a very good agreement between the two numerical simulations can be observed along the three reference axes, with regard to both displacement and stress components.

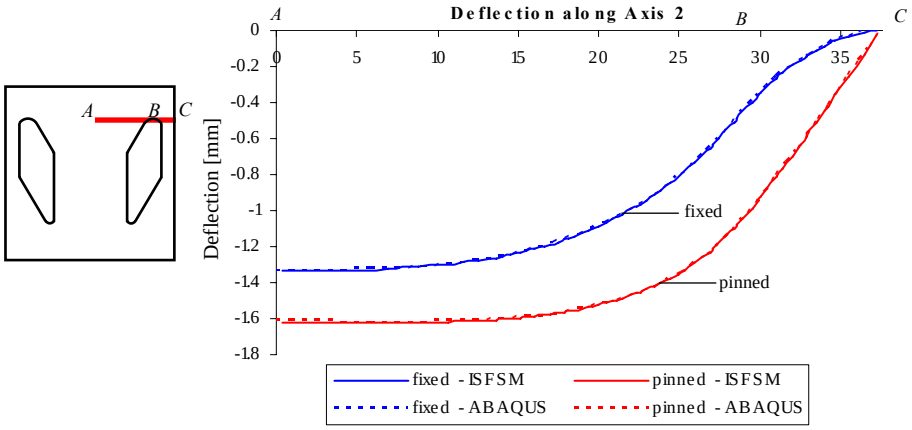

Fig. 29: Diamond perforations, deflection comparison along axis 2.

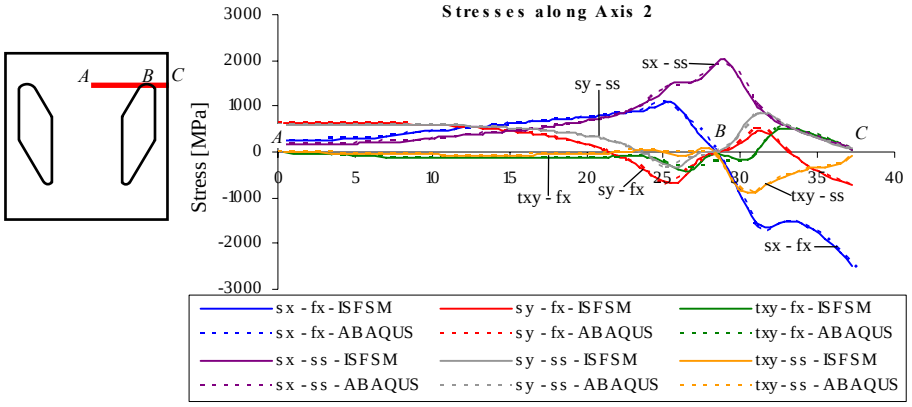

Fig. 30: Diamond perforations, stress comparison along axis 2.

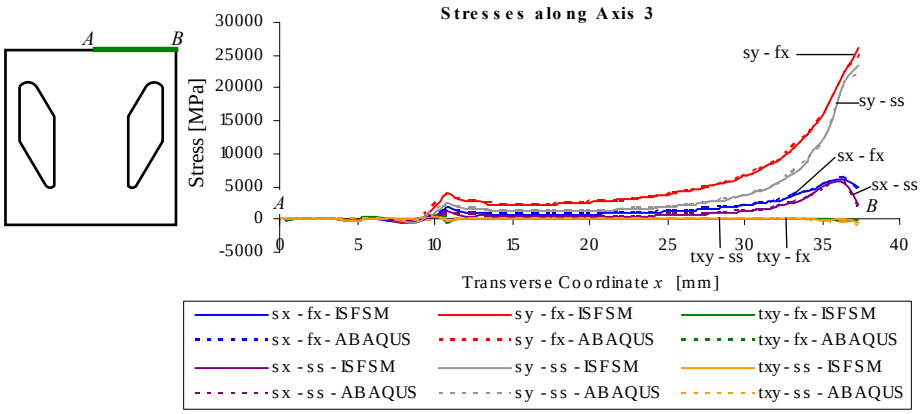

Fig. 31: Diamond perforations, stress comparison along axis 3.

Conclusions

The application of the isoparametric spline finite strip method to the bending of perforated plates has been presented. The linear elastic Mindlin plate bending theory has been presented in detail and the relevant strain and stiffness spline finite strip matrices have been set out.

A number of examples have demonstrated the accuracy of the isoparametric spline finite strip method in dealing with challenging problems like the stress amplification in plates with perforations of different shape. The

examples have included perforations with both rounded and sharp corners. The accuracy of the results has been assessed against finely meshed finite element analyses.

The comparison of the results has shown that a good representation of the displacements and stress distributions can be obtained with the isoparametric spline finite strip method using a small number of strips and a relatively small number of nodes compared to the number of elements and nodes required by the finite element analysis.

References

[1] Eccher, G, Rasmussen, KJR, Baldassino, N, Zandonini, R. Isoparametric Spline Finite Strip Method for In-plane Stress Analysis. The University of Sydney, Department of Civil Engineering, R848, 2005.

[2] Cheung, YK. Finite strip method in structural analysis. Oxford ; New York: Pergamon Press, 1976.

[3] Cheung, YK, Fan, SC, Wu, CQ. Spline finite strip in structural analysis. In: editors. Proceedings of the Proceedings of the International Conference on Finite Element Method. Shanghai, China: 1982

[4] Fan, SC, Spline finite strip in structural analysis., Thesis, University of Hong Kong, 1982.

[5] Au, FTK, Cheung, YK. Isoparametric spline finite strip for plane structures. Computers & Structures 1993; 48(1):23-32.

[6] Cheung, YK, Au, FTK. Isoparametric spline finite strip for degenerate shells. Thin-Walled Structures 1995; 21(1):65-92.

[7] Godley, MHR. Storage Racking - chapter 11. In: editors. Design of Cold Formed Steel Members. Ed. Rhodes, 1991.

[8] Shanmugam, NE, Thevendran, V, Tan, YH. Design formula for axially compressed perforated plates. Thin-Walled Structures 1999; 34(1):1.

[9] Shanmugam, NE, Thevendran, V. Lateral buckling of doubly symmetric beams containing openings. Journal of Engineering Mechanics, American Society of Civil Engineers 1991; 117(7):1427-1441.

[10] Shanmugam, NE, Dhanalakshmi, M. State of art review and compilation of studies on perforated thin-walled structures. International Journal of Structural Stability and Dynamics 2001; 1

[11] Rhodes, J, Macdonald, M. The effect of perforation length on the behaviour of perforated elements in compression. In: editors. Proceedings of the Thirthteenth International Speciality Conference on Cold-Formed Steel Structures. 1996

[12] Eccher, G, Rasmussen, KJR, Zandonini, R. Shear locking in isoparametric spline finite strips. School of Civil Engineering, The University of Sydney, Sydney, Australia, R876, 2007.

[13] ABAQUS/STANDARD. User's Manual Version 6.5. Hibbit, USA: Karlsson & Sorensen, 2006.